Photocatalytic Activity of R$_3$MO$_7$ and R$_2$Ti$_2$O$_7$ (R = Y, Gd, La; M = Nb, Ta) for Water Splitting into H$_2$ and O$_2$

Ryu Abe,*,† Masanobu Higashi,‡ Kazuhiro Sayama,† Yoshimoto Abe,‡ and Hideki Sugihara†

National Institute of Advanced Industrial Science and Technology (AIST),
1−1−1 Higashi, Tsukuba, Ibaraki 305-8565, Japan, and Faculty of Science and Technology,
Tokyo University of Science, Yamazaki 2641, Noda, Chiba 278-8514, Japan

The photocatalytic activities of R$_3$MO$_7$ and R$_2$Ti$_2$O$_7$ (R = Y, Gd, La; M = Nb, Ta) strongly depended on the crystal structure. Overall, photocatalytic water splitting into H$_2$ and O$_2$ proceeded over La$_3$TaO$_7$ and La$_3$NbO$_7$, which have an orthorhombic weberite structure, Y$_2$Ti$_2$O$_7$ and Gd$_2$Ti$_2$O$_7$, which have a cubic pyrochlore structure, and La$_2$Ti$_2$O$_7$, which has a monoclinic perovskite structure. All of these materials are composed of a network of corner-shared octahedral units of metal cations (TaO$_6$, NbO$_6$, or TiO$_6$); materials without such a network were inactive. The octahedral network certainly increased the mobility of electrons and holes, thereby enhancing photocatalytic activity.

1. Introduction

Photocatalytic water splitting into H$_2$ and O$_2$ by semiconducting catalysts has received much attention owing to its potential for producing clean H$_2$ fuel from water by using solar energy.[1−19] Photocatalysis on semiconductors occurs in three main steps: (i) adsorption of photons corresponding to the energy band gap of the material, leading to generation of electron−hole pairs in the semiconductor particles, (ii) charge separation and migration of photogenerated carriers in the semiconductor particles, and (iii) surface chemical reactions between these carriers with various substances. Although the second step is certainly associated with the crystal structure of the semiconductor, it has received little attention so far. To determine the effect of crystal structure on photocatalytic activity, a variety of materials with different crystal structures need to be evaluated. However, only a limited number of photocatalysts have been identified so far, and most of the active materials are perovskite-type compounds, such as SrTiO$_3$,[2,3] K$_2$-La$_2$Ti$_3$O$_{10}$,[7] KTaO$_3$,[9] NaTaO$_3$,[13] Sr$_2$M$_2$O$_7$ (M = Ta, Nb),[8,11] RbNdTa$_2$O$_7$,[10] and La$_2$Ti$_2$O$_7$.[8,14]

In the present study, we have chosen R$_3$MO$_7$ and R$_2$Ti$_2$O$_7$ (R = Y, Gd, La; M = Nb, Ta) systems as photocatalysts for water splitting.[15,16] It has been reported that the distortion in the crystal structure of R$_3$TaO$_7$ (R = rare earth) increases with the ionic radius of R^{3+}, changing from a cubic fluorite structure to a cubic pyrochlore structure, then finally to an orthorhombic weberite structure.[20,21] R$_2$Ti$_2$O$_7$ materials possess a cubic pyrochlore structure with small R^{3+} ions (Yb^{3+}−Sm^{3+}), while R$_2$Ti$_2$O$_7$ with their larger R^{3+} (Nd^{3+}−La^{3+}) exhibit a monoclinic perovskite structure.[14,22,23] The relationship between the photocatalytic activities of these materials and their crystal structures was discussed.

2. Experimental Procedures

2.1. Materials. Powder samples of R$_3$MO$_7$ and R$_2$Ti$_2$O$_7$ (R = Y, Gd, La; M = Nb, Ta) were prepared by a polymerized complex (PC) method; the preparation basically followed the previous reports on Y$_3$NbO$_7$, Y$_2$Ti$_2$O$_7$, and La$_2$Ti$_2$O$_7$ by Kakihana et al.[23−25] In the case of R$_3$MO$_7$, methanol (ca. 25 mL) was used as a solvent to dissolve 0.01 mol of TaCl$_5$ or NbCl$_5$. A large excess of citric acid (CA, ca. 0.3 mol) was added into the methanol solution of TaCl$_5$ or NbCl$_5$ with continuous stirring to produce metal−CA complexes. Once the CA was completely dissolved in the methanol solution, 0.03 mol of R(NO$_3$)$_3$·nH$_2$O (R = Y, Gd, La) was added, and the mixture was magnetically stirred for 1 h to produce a transparent solution of the metal−CA complexes. Subsequently, 0.4 mol of ethylene glycol (EG) was added to this solution. The clear solution thus prepared was heated at ∼130 °C to remove the methanol and accelerate esterification reactions between CA and EG. Upon continuous heating at ca. 130 °C, the solution became highly viscous with a change in color from colorless to deep brown and, finally, gelled into a transparent-brown glassy resin. The resin was charred in an electric furnace for 2 h at ca. 350 °C. The resulting black solid mass was calcined on an Al$_2$O$_3$ plate at 800−1350 °C for 2−4 h in static air, followed by natural (furnace) cooling to room temperature. In the case of R$_2$Ti$_2$O$_7$, 0.01 mol of titanium isopropoxide (Ti[OCH(CH$_3$)$_2$]$_4$) was first dissolved in 0.4 mol of EG. Subsequently, 0.3 mol of CA was added to the solution with continuous stirring. After complete dissolution of the CA, 0.0105 mol (5% excess to Ti) of R$_3$(NO$_3$)$_3$·nH$_2$O was added to the solution. Excess R^{3+} was added to prevent formation of the impurity TiO$_2$ rutile, which forms on the surface of R$_2$Ti$_2$O$_7$ materials at high temperature and thereby decreases photocatalytic activity.[26] The remaining procedures were the same as those followed in the preparation of R$_3$MO$_7$ described above.

2.2. Characterization. The synthesized materials were confirmed by powder X-ray diffraction (MAC science, MX Lab.). Raman spectra of the materials were collected by using a laser Raman spectrophotometer (Jasco, NRS-1000, with green diode laser at 532 nm). The surface area was determined by

* Corresponding author. E-mail: ryu-abe@cat.hokudai.ac.jp. Present address: Catalyst Research Center, Hokkaido University, Sapporo 001-0021, Japan.
† National Institute of Advanced Industrial Science and Technology (AIST).
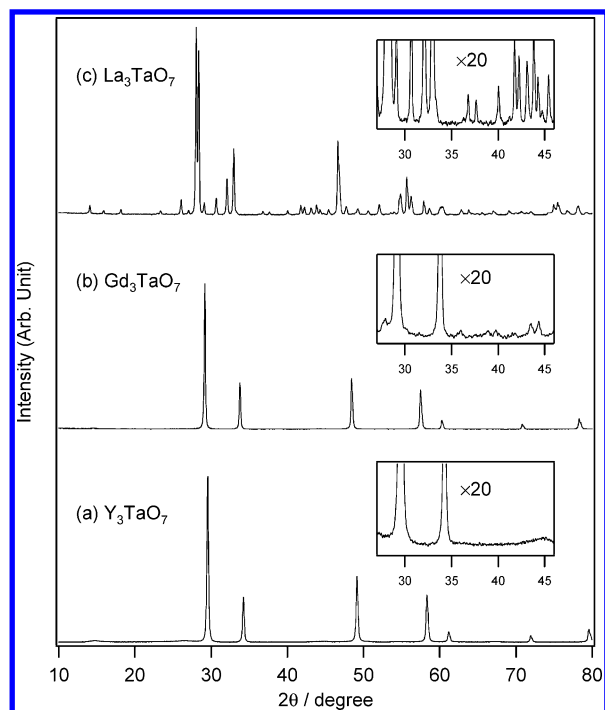‡ Faculty of Science and Technology, Tokyo University of Science.

Figure 1. X-ray diffraction patterns of (a) Y_3TaO_7, (b) Gd_3TaO_7, and (c) La_3TaO_7 prepared by the polymerized complex method following calcination at 1350 °C for 4 h.

BET surface area measurement (Shimadzu, Gemini 2360). Diffuse reflectance spectra were obtained by using a UV−vis spectrometer (Jasco, V-570) and were converted from reflection to absorbance by the Kubelka−Munk method.

2.3. Photocatalytic Reaction. A NiO_x cocatalyst was loaded on the photocatalyst powder to promote H_2 production.[27] The photocatalyst powder prepared by the PC method was immersed into an aqueous solution containing the required amount of $Ni(NO_3)_2$. The solution was then evaporated to a dry solid by using a water bath, followed by heating in air at ca. 300 °C for 20 min. The NiO-supported photocatalyst was then reduced in flowing H_2 at 500 °C for 2 h and subsequently oxidized at 200 °C for 1 h in air to get a NiO_x-supported photocatalyst. The photocatalytic reaction was examined by using a closed gas circulation system. The photocatalyst powder (0.5 g) was dispersed in distilled water (400 mL) by a magnetic stirrer in an inner-irradiation-type reaction cell. The light source (400 W high-pressure mercury lamp, Riko Kagaku, Japan) was covered with a water jacket (quartz glass, cutoff λ < 200 nm) to keep the reactor temperature constant at 20 °C by using cooling water. The suspension was thoroughly degassed. Argon gas (35 Torr) was introduced into the system, and then the suspension was exposed to irradiation. The gases released were analyzed by on-line gas chromatography (TCD, molecular sieve 5A, Ar carrier).

3. Results and Discussion

3.1. XRD Patterns and Raman Spectra of R_3TaO_7 and R_3NbO_7 Samples. Figure 1 shows the X-ray diffraction (XRD) patterns of R_3TaO_7 samples (R = Y, Gd, La) prepared by the PC method at 1350 °C in 4 h. The XRD pattern of Y_3TaO_7 containing the smaller Y^{3+} ion (0.88 A) was typical for a cubic fluorite structure. In the diffraction patterns of Gd_3TaO_7 and La_3TaO_7, with the larger Gd^{3+} ions (0.94 A) and La^{3+} ions (1.06 A), respectively, several superlattice lines appeared; the diffraction peaks of the fundamental lines were split. They were
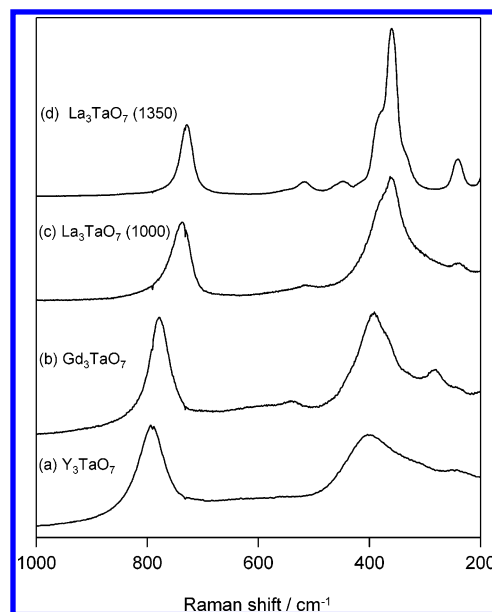

Figure 2. Raman spectra of (a) Y_3TaO_7, (b) Gd_3TaO_7, (c) La_3TaO_7 prepared at 1000 °C, and (d) La_3TaO_7 prepared at 1350 °C.

indicative of a cubic pyrochlore (Gd_3TaO_7) and an orthorhombic weberite structure (La_3TaO_7). These XRD patterns of the samples prepared by the PC method were identical to those of the samples prepared by solid-state reactions at 1700 °C in 4 h or at 1350 °C in 96 h by Yokogawa et al.[21,22] XRD patterns observed for R_3NbO_7 samples were similar to those for R_3TaO_7, except for a slight difference in lattice parameters. This indicates that the crystal structure of Y_3NbO_7, Gd_3NbO_7, and La_3NbO_7 are cubic fluorite, cubic pyrochlore, and orthorhombic weberite, respectively.[28,29]

Raman spectra of R_3TaO_7 (R = Y, Gd, La) samples prepared at 1350 °C and the La_3TaO_7 sample prepared at 1000 °C are shown in Figure 2. Two broad Raman bands are observed in the 700−900 and 200−500 cm^{-1} ranges for Y_3TaO_7 with a cubic fluorite structure, as shown in Figure 2a. As for Gd_3TaO_7 with its cubic pyrochlore structure (Figure 2b), the bands at ∼400 cm^{-1} are sharper than those in Y_3TaO_7, and additional bands appear at ∼530 and ∼290 cm^{-1}. Strong multiple Raman bands are observed in the wavenumber range 200−700 cm^{-1} for La_3TaO_7 with an orthorhombic weberite structure (Figure 2d). The main Raman bands at around 660 and 290 cm^{-1} are possibly assigned to Ta−O stretching and Ta−O−Ta bending modes in the La_3TaO_7, respectively, and these bands were observed at a lower wavenumber in the case of weberite−La_3NbO_7 (Figure 6).[30] As shown in Figure 1, the cubic fluorite (Y_3TaO_7) and cubic pyrochlore (Gd_3TaO_7) structures are difficult to distinguish from their XRD patterns because the intensities of the characteristic peaks of the pyrochlore structure are quite low. On the other hand, the Raman spectrum of Gd_3TaO_7 is clearly different from that of Y_3TaO_7.

3.2. Phase Transition of La_3TaO_7 and La_3NbO_7 Prepared by the PC Method. Our detailed investigation into the preparation of La_3TaO_7 and La_3NbO_7 samples by the PC method revealed that their phase transition from cubic pyrochlore to orthorhombic weberite occurred at around 1050 and 1000 °C, respectively. As shown in Figure 3, the XRD patterns of some La_3TaO_7 samples prepared below 1000 °C exhibited a typical cubic structure like Y_3TaO_7 or Gd_3TaO_7, while those above 1100 °C indicate orthorhombic weberite structure. The phase transition was also confirmed by Raman spectra of La_3TaO_7 samples prepared at various temperatures, as shown in Figure 4. Raman
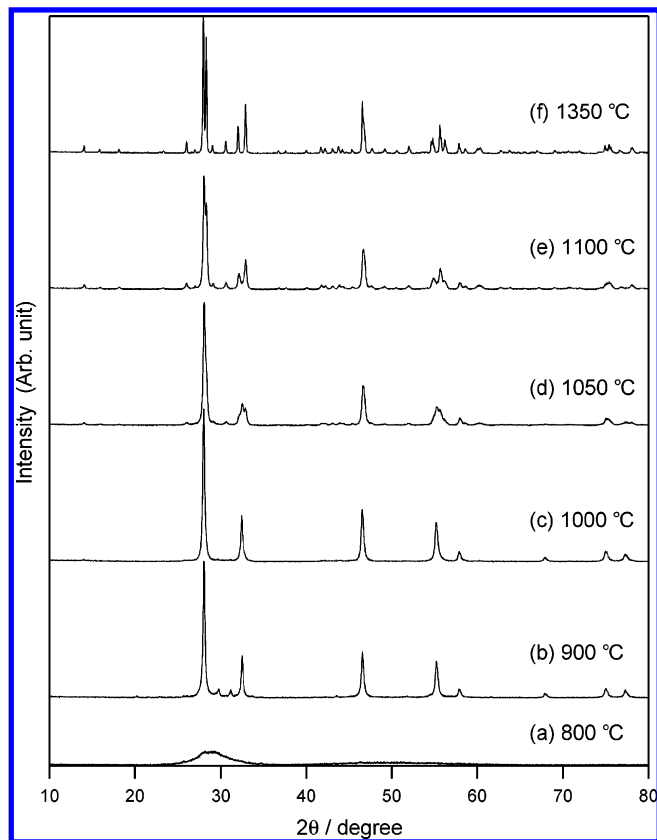
Figure 3. X-ray diffraction patterns of La$_3$TaO$_7$ samples prepared by the polymerized complex method following a four-hour calcination run in air at various temperatures ranging from 800 to 1350 °C.
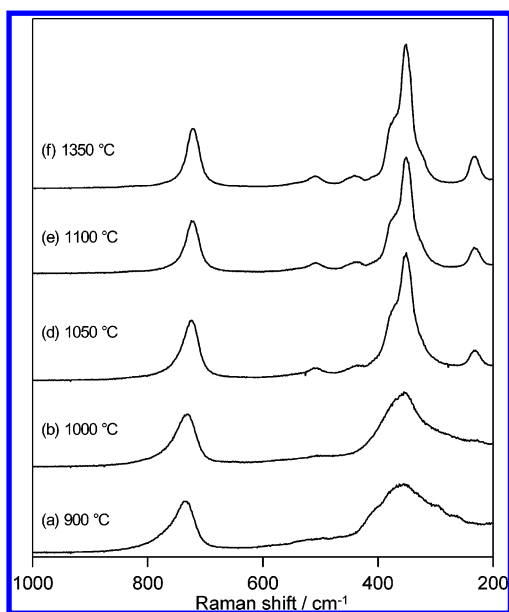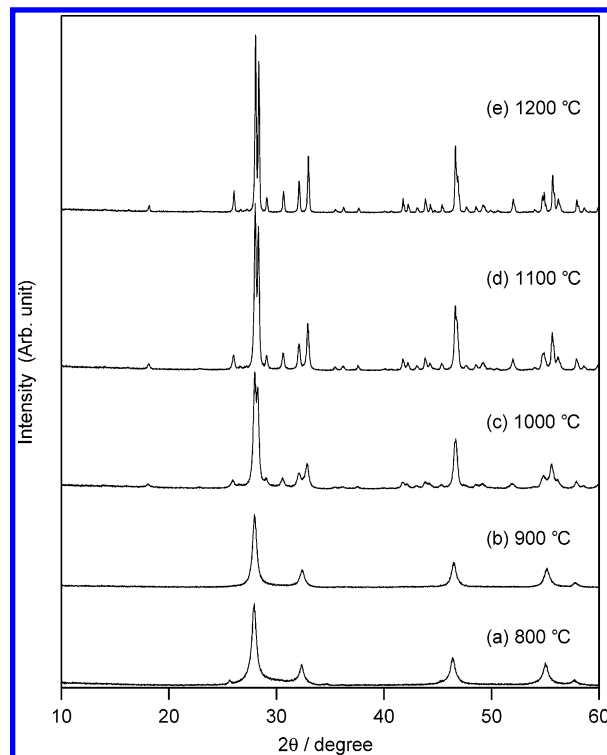

Figure 5. X-ray diffraction patterns of La$_3$NbO$_7$ samples prepared by the polymerized complex method following a four-hour calcination run in air at various temperatures ranging from 800 to 1200 °C.

Figure 4. Raman spectra of La$_3$TaO$_7$ samples prepared by the polymerized complex method following a four-hour calcination run in air at various temperatures ranging from 900 to 1350 °C.

Figure 6. Raman spectra of La$_3$NbO$_7$ samples prepared by the polymerized complex method following a four-hour calcination run in air at various temperatures ranging from 800 to 1200 °C.
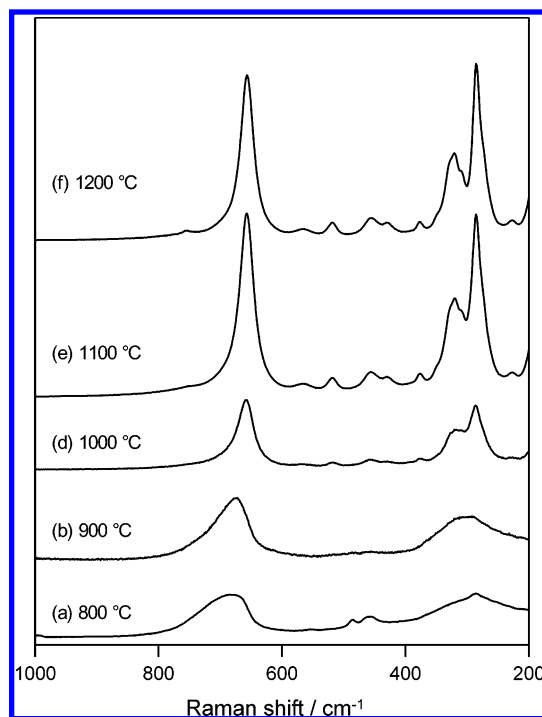
bands at ~230, ~430, and ~500 cm^{-1}, which show an orthorhombic weberite structure, are clearly observed in La$_3$-TaO$_7$ samples prepared at above 1050 °C. In the case of La$_3$-NbO$_7$, the phase transition was observed at around 1000 °C, as shown in the XRD patterns (Figure 5) and the Raman spectra (Figure 6). Although the La$_3$NbO$_7$ sample prepared at 800 °C still contains some impurity phase of Nb$_2$O$_5$ and La$_2$O$_3$, the XRD pattern and Raman spectrum of the La$_3$NbO$_7$ prepared at 900 °C indicate pure cubic structure. On the other hand, the La$_3$-

NbO$_7$ samples prepared above 1000 °C indicate orthorhombic weberite structure. As described in the previous section, the structures of cubic materials are difficult to determine through XRD patterns. However, the Raman spectrum of the La$_3$TaO$_7$ prepared at 1000 °C is quite similar to that of Gd$_3$TaO$_7$ with a cubic pyrochlore structure, as shown in Figure 2. Thus, the low-temperature La$_3$TaO$_7$, as well as La$_3$NbO$_7$, possibly possess a cubic pyrochlore structure. To the best of our knowledge, the
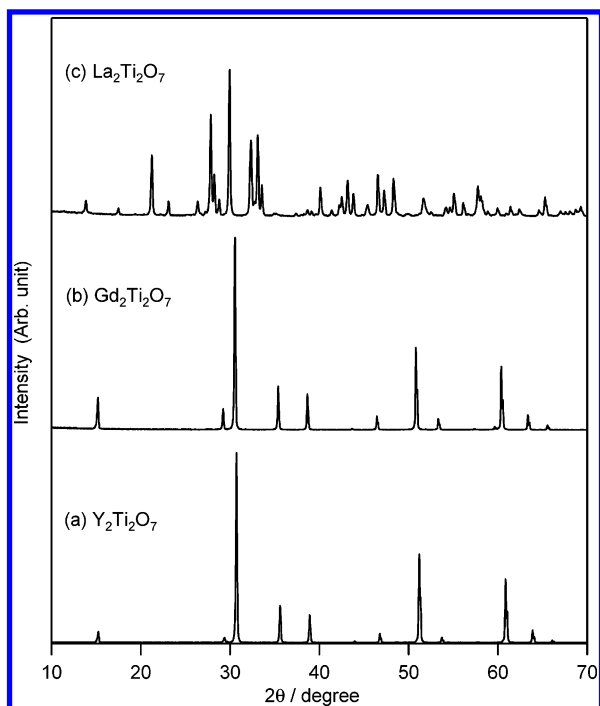
Figure 7. X-ray diffraction patterns of (a) $Y_2Ti_2O_7$, (b) $Gd_2Ti_2O_7$, and (c) $La_2Ti_2O_7$ prepared by the polymerized complex method following calcination at 1000 °C for 2 h.

Figure 8. Raman spectra of (a) $Y_2Ti_2O_7$, (b) $Gd_2Ti_2O_7$, and (c) $La_2Ti_2O_7$ prepared by the polymerized complex method following calcination at 1000 °C for 2 h.

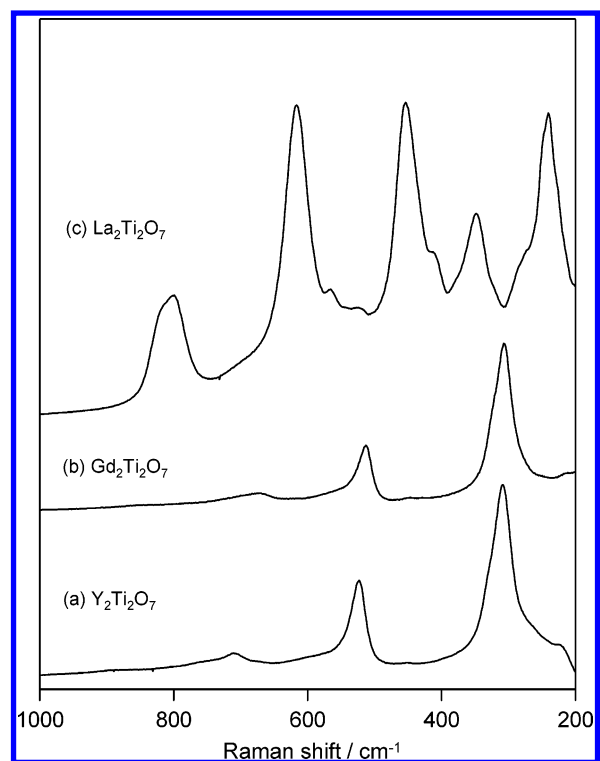synthesis of cubic La_3TaO_7 and La_3NbO_7 through traditional solid-state reactions has not been reported. Low-temperature synthesis by the PC method enables the generation of the cubic phase.

3.3. XRD Patterns and Raman Spectra of $R_2Ti_2O_7$ Samples. Figure 7 shows the XRD patterns of the $R_2Ti_2O_7$ (R = Y, Gd, La) samples prepared by the PC method at 1000 °C in 2 h. The XRD patterns of $Y_2Ti_2O_7$ and $Gd_2Ti_2O_7$ containing
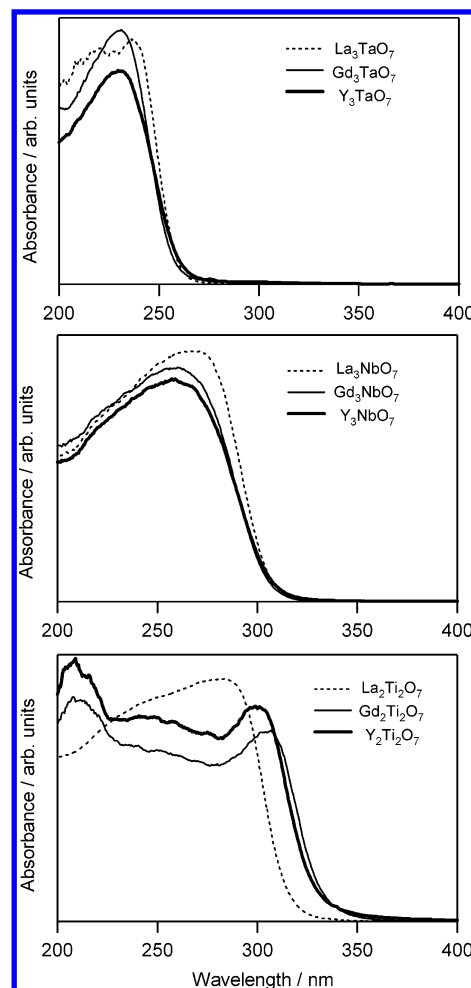
Figure 9. Diffuse reflection spectra of R_3MO_7 and $R_2Ti_2O_7$ (R = Y, Gd, La; M = Nb, Ta), prepared at 1350 °C in 4 h and at 1000 °C in 2 h, respectively.

the smaller R^{3+} ions have a typical cubic pyrochlore structure. On the other hand, the XRD pattern of $La_2Ti_2O_7$ with the larger La^{3+} ion shows a monoclinic perovskite structure. These results agree with previous reports on $R_2Ti_2O_7$ materials prepared by a solid-state reaction, in which $R_2Ti_2O_7$ materials containing R^{3+} ions smaller than Sm^{3+} possess a cubic pyrochlore structure, while those containing R^{3+} ions larger than Nd^{3+} exhibit a monoclinic perovskite structure.[14,22−24] Raman spectra of the $Y_2Ti_2O_7$, $Gd_2Ti_2O_7$, and $La_2Ti_2O_7$ samples are shown in Figure 8. The spectral shapes of $Y_2Ti_2O_7$ and $La_2Ti_2O_7$ are quite different and are characteristic of the cubic pyrochlore[31] and monoclinic perovskite structures, respectively.

3.4. Diffuse Reflection Spectra of R_3MO_7 and $R_2Ti_2O_7$ (R = Y, Gd, La; M = Nb, Ta). Diffuse reflection spectra of the prepared materials are shown in Figure 9. In the case of R_3-TaO_7 and R_3NbO_7 systems, the spectra are similar regardless of the R^{3+} ion, and the band gaps of R_3TaO_7 and R_3NbO_7 samples estimated from the onset of the diffuse reflection spectra are ca. 4.6 and 3.9 eV, respectively. Figure 10 shows the diffuse reflection spectra of the La_3TaO_7 samples with different crystal structures, orthorhombic weberite (a) and cubic pyrochlore (b), prepared by calcination at 1100 and 1000 °C, respectively. The two spectra are almost identical. These results indicate that the effect of the R^{3+} ion on the band structure is not so significant in R_3MO_7.

On the other hand, the diffuse reflection spectra of $R_2Ti_2O_7$ vary with crystal structure (cubic pyrochlore or monoclinic perovskite), as shown in Figure 9. The estimated band gap of

TABLE 1: Photocatalytic Activities for Water Splitting and Crystal Structures of Prepared Materials

photocatalyst[a]	calcination temp (°C)	type of structure	rate of gas evolution (μmol h^{-1})[b]		surface area (m^2 g^{-1})	band gap (eV)
			H$_2$	O$_2$		
Y$_3$TaO$_7$	1350	cubic fluorite	tr	0	1.6	4.6
Gd$_3$TaO$_7$	1350	cubic pyrochlore	2	0	2.3	4.6
La$_3$TaO$_7$	1000	cubic pyrochlore	4	0	3.0	4.6
La$_3$TaO$_7$	1100	orthorhombic weberite	164	80	2.8	4.6
Y$_3$NbO$_7$	1350	cubic fluorite	tr	0	1.2	3.9
Gd$_3$NbO$_7$	1350	cubic pyrochlore	0.5	0	3.0	3.9
La$_3$NbO$_7$	900	cubic pyrochlore	1	0	2.8	3.9
La$_3$NbO$_7$	1100	orthorhombic weberite	35	17	2.5	3.9
Y$_2$Ti$_2$O$_7$	1000	cubic pyrochlore	850	420	2.0	3.5
Gd$_2$Ti$_2$O$_7$	1000	cubic pyrochlore	400	198	2.3	3.5
La$_2$Ti$_2$O$_7$	1000	monoclinic perovskite	307	152	1.8	3.8

[a] NiO$_x$ loaded: 1 wt %. [b] Catalyst = 0.5 g; distilled water = 400 mL; light source = 400 W high-pressure mercury lamp; reaction cell = inner irradiation cell made of quartz.
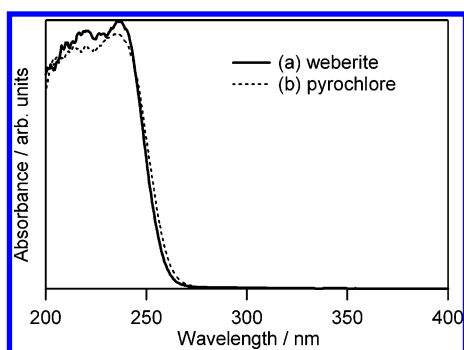

Figure 10. Diffuse reflection spectra of (a) orthorhombic weberite La$_3$-TaO$_7$ prepared at 1100 °C in 4 h and (b) cubic pyrochlore La$_3$TaO$_7$ prepared at 1000 °C in 4 h.

La$_2$Ti$_2$O$_7$ (3.8 eV) with a monoclinic perovskite structure is larger than those of Y$_2$Ti$_2$O$_7$ and Gd$_2$Ti$_2$O$_7$ (3.5 eV) with cubic pyrochlore structure.

3.5. Photocatalytic Activities of R$_3$MO$_7$ and R$_2$Ti$_2$O$_7$ (R = Y, Gd, La; M = Nb, Ta) for Overall Water Splitting into H$_2$ and O$_2$. The photocatalytic activities of NiO$_x$-loaded R$_3$MO$_7$ and R$_2$Ti$_2$O$_7$ samples for the splitting of distilled water and their crystal structures are summarized in Table 1. As for R$_3$MO$_7$ systems, La$_3$TaO$_7$ and La$_3$NbO$_7$ with orthorhombic weberite structure exhibited activities for simultaneous evolution of H$_2$ and O$_2$ in the stoichiometric ratio (H$_2$/O$_2$ = 2:1). On the other hand, only a small amount of H$_2$, but no O$_2$, was released over the other photocatalysts with cubic fluorite or cubic pyrochlore structures. The rate of H$_2$ and O$_2$ evolution over the NiO$_x$–La$_3$TaO$_7$ samples are plotted as a function of the calcination temperature in Figure 11, wherein data for the specific surface area of each sample is also shown. The rate of gas evolution increased dramatically with increasing calcination temperature from 1000 to 1100 °C. It was in this temperature range that the phase transition from cubic pyrochlore to orthorhombic weberite structure occurred, as shown in Figures 3 and 4. The rate of gas evolution gradually decreased above 1100 °C. The decrease was possibly due to the decrease in surface area, as shown in Figure 11. A similar trend was observed for NiO$_x$–La$_3$NbO$_7$ photocatalysts. As shown in Figure 12, the rate of gas evolution significantly increased with the phase transition of La$_3$NbO$_7$. Figure 13 shows the time courses of gas evolution over NiO$_x$ (1 wt %)-loaded La$_3$TaO$_7$ photocatalysts prepared at 1100 °C ((a) orthorhombic weberite) and 1000 °C ((b) cubic pyrochlore), and over NiO$_x$ (1 wt %)-loaded La$_3$NbO$_7$ photocatalysts prepared at 1100 °C ((c) orthorhombic weberite) and 900 °C ((d) cubic pyrochlore). The La$_3$TaO$_7$ and La$_3$NbO$_7$ samples with
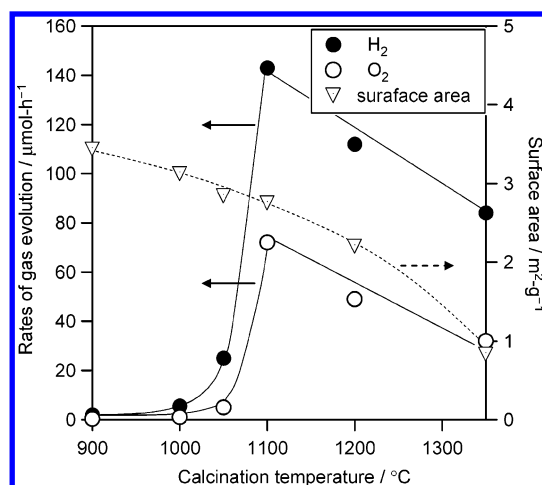

Figure 11. The rates of gas evolution and the specific surface area of 1 wt % NiO$_x$–La$_3$TaO$_7$ samples as a function of calcination temperature.
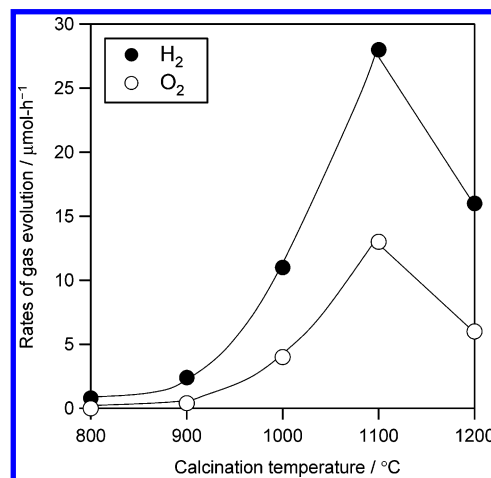

Figure 12. The rates of gas evolution over 1 wt % NiO$_x$–La$_3$NbO$_7$ samples as a function of calcination temperature.

orthorhombic weberite structure exhibited a much higher activity than those with a cubic pyrochlore structure. These results clearly indicate that it is the crystal structure, rather than the constituent elements, that determines the photocatalytic activity of R$_3$MO$_7$ systems. The difference in the crystal structure might change the conduction and valence band levels of the semiconductor materials. However, the conduction band levels of the tantalate semiconductors, which are mainly formed by the Ta-5d orbital, are generally negative enough to reduce water into H$_2$. Furthermore, the valence band levels of oxide semi-
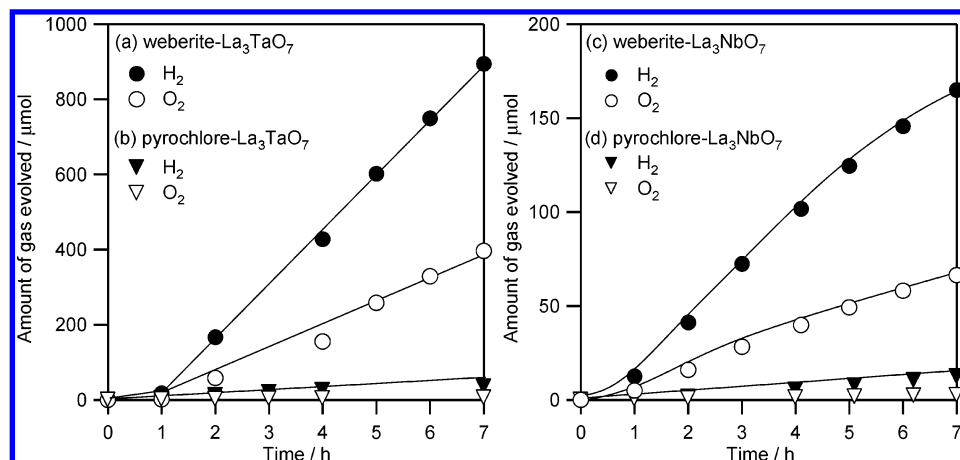
Figure 13. Reaction time course of gas evolution from distilled water (400 mL) over 1 wt % NiO$_x$-loaded photocatalysts under UV irradiation: (a) orthorhombic weberite La$_3$TaO$_7$ prepared at 1100 °C, (b) cubic pyrochlore La$_3$TaO$_7$ prepared at 1000 °C, (c) orthorhombic weberite La$_3$NbO$_7$ prepared at 1100 °C, and (d) cubic pyrochlore La$_3$NbO$_7$ prepared at 900 °C.
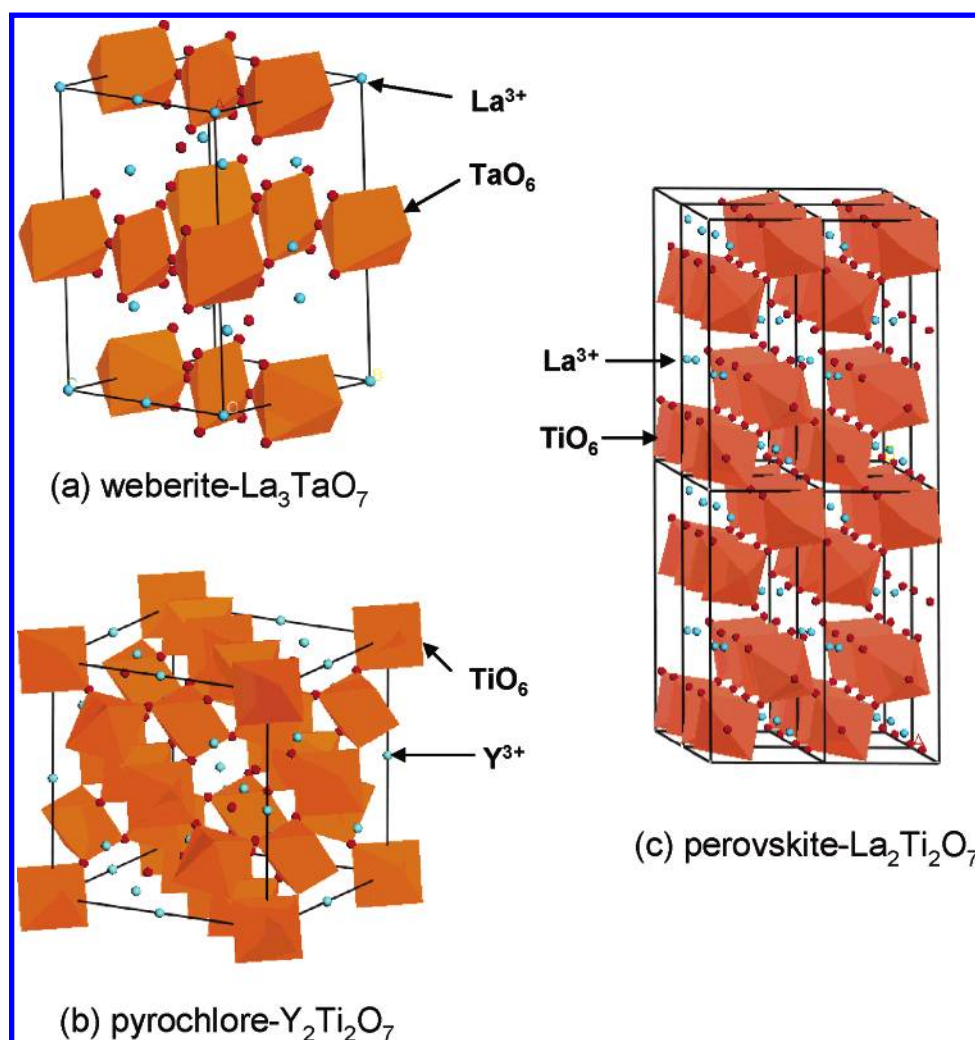

Figure 14. Schematic drawing of (a) weberite La$_3$TaO$_7$, (b) pyrochlore Y$_2$Ti$_2$O$_7$, and (c) perovskite La$_2$Ti$_2$O$_7$.

conductors are generally much more positive than the oxidation potential of water.[13,32] Therefore, the photocatalytic activity of R$_3$TaO$_7$ materials for water splitting would not be influenced significantly by the change in the band levels, if the change occurred.

As for the R$_2$Ti$_2$O$_7$ system, both of the photocatalysts with cubic pyrochlore structure (Y$_2$Ti$_2$O$_7$, Gd$_2$Ti$_2$O$_7$) and the photocatalyst with monoclinic perovskite structure (La$_2$Ti$_2$O$_7$) exhibited simultaneous evolution of H$_2$ and O$_2$ in the stoichio-

metric ratio, as shown in Table 1. As described in the Introduction, various perovskite-type materials, including La$_2$-Ti$_2$O$_7$, have already been reported to show photocatalytic activity for overall water splitting.[8,14] However, we have demonstrated for the first time that a photocatalyst with pyrochlore structure exhibited activity for efficient overall water splitting.[16,26]

3.6. Effect of Crystal Structure on Photocatalytic Activity. The crystal structures of the photocatalysts that exhibited activity for overall water splitting are shown in Figure 14. The
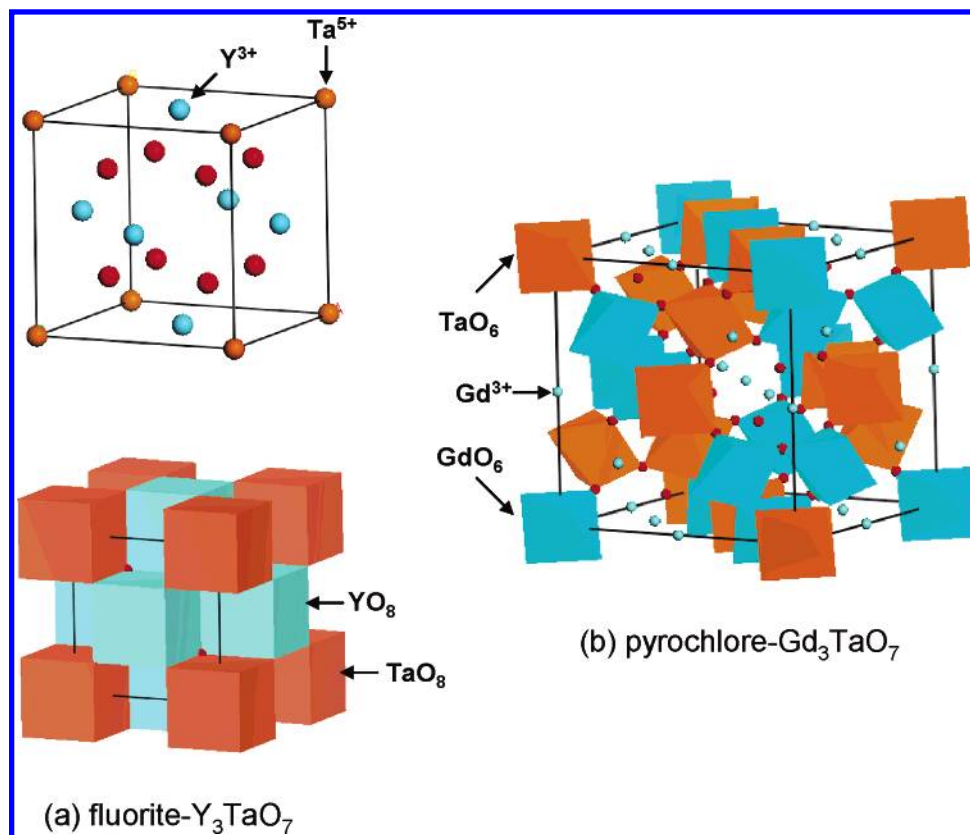
Figure 15. Schematic drawing of (a) fluorite Y$_3$TaO$_7$ and (b) pyrochlore Gd$_3$TaO$_7$.

orthorhombic weberite La$_3$TaO$_7$ (or La$_3$NbO$_7$) (Figure 14a) consists of zigzag chains formed by corner-shared TaO$_6$ (or NbO$_6$) octahedrons.[28] The chains are linked at their corners with a network formed by OLa$_4$ tetrahedrons. As shown in Figure 14b, the cubic pyrochlore titanate Y$_2$Ti$_2$O$_7$ (or Gd$_2$Ti$_2$O$_7$) consists of a three-dimensional network of octahedral TiO$_6$ connected at their corners, forming a three-dimensional network of zigzag chains; the Y (or Gd) ions are located within this network.[22,29] La$_2$Ti$_2$O$_7$ (Figure 14c) is a member of a homologous series of layered structures built from (110) perovskite slabs formed by corner-shared TiO$_6$ octahedrons and La ions.[14,22] Adjacent slabs are staggered by half of a TiO$_6$ octahedron height, and the octahedron connectivity is broken at the shear interface. Clearly, the above materials that exhibited high photocatalytic activity are composed of chains or slabs formed by corner-shared octahedral units of metal cations (TaO$_6$, NbO$_6$, or TiO$_6$), which contribute mainly to the conduction band of the semiconductor.

Figure 15 shows the crystal structures of the materials that are inactive for an overall water-splitting reaction. The XRD patterns of Y$_3$TaO$_7$ and Y$_3$NbO$_7$ are quite similar to that of Yb$_3$TaO$_7$, which was reported to have a fluorite phase.[21] On this basis, we assumed that the crystal structures of Y$_3$TaO$_7$ and Y$_3$NbO$_7$ are identical to that of Yb$_3$TaO$_7$, as shown in Figure 15a, where Y, Ta (or Nb), and O ions are located at the face-center, corner, and anion sites, respectively. In this case, the octahedral units of TaO$_6$ (or NbO$_6$) that were observed in the active materials were not formed. Another schematic drawing of Y$_3$TaO$_7$ is shown in Figure 15a, in which the TaO$_8$ and YO$_8$ units are alternately linked by corner sharing. It is expected that the cubic pyrochlore Gd$_3$TaO$_7$ (or Gd$_3$NbO$_7$) will have a crystal structure similar to that of the cubic pyrochlore Y$_2$Ti$_2$O$_7$, a pyrochlore material with the empirical formula A$_2$B$_2$O$_7$. However, in the case of Gd$_3$TaO$_7$, the B sites must be occupied with both TaO$_6$ and GdO$_6$ octahedrons at the ratio of 1:1. Figure 15b shows the expected crystal structure of cubic pyrochlore

Gd$_3$TaO$_7$, by assuming an arrangement of alternating octahedral units of TaO$_6$ and GdO$_6$ in the B sites. In this case, the three-dimensional network is formed by a mixture of TaO$_6$ and GdO$_6$ octahedrons. The XRD and Raman results indicate that La$_3$TaO$_7$ prepared at low temperature would have a crystal structure similar to that of cubic pyrochlore Gd$_3$TaO$_7$.

Let us consider the effect of crystal structure on photocatalytic activity. As indicated above, all of the active photocatalysts possess chains or slabs formed by corner-shared octahedral units of metal cations, such as TaO$_6$, NbO$_6$, or TiO$_6$. On the other hand, such chains of octahedral units are not formed in the inactive materials with a fluorite-cubic structure (Y$_3$TaO$_7$ and Y$_3$NbO$_7$). Although chains of octahedral units are formed in the inactive materials with a cubic pyrochlore structure (Gd$_3$-TaO$_7$, Gd$_3$NbO$_7$, La$_3$TaO$_7$, and La$_3$NbO$_7$), the chains consist of a mixture of octahedral units of metal cations (TaO$_6$ or NbO$_6$) and lanthanides (GdO$_6$ or LaO$_6$). From these results, we can conclude that the network, chains or slabs, formed by corner-shared octahedral units of TaO$_6$, NbO$_6$, or TiO$_6$, are essential for these semiconductors to exhibit high photocatalytic activity. The network of octahedrons certainly increases the mobility of the charged particles, namely electrons and holes, in the materials. West et al. have synthesized various mixed oxides in the system ZrO$_2$−La$_2$O$_3$−Ta$_2$O$_5$, including the weberite La$_3$TaO$_7$, and evaluated their electrochemical conductivity.[33] They have reported that both the crystal structure and composition significantly affect the electrochemical conductivity, and that the weberite La$_3$TaO$_7$ exhibited relatively high conductivity among the mixed oxides in the ZrO$_2$−La$_2$O$_3$−Ta$_2$O$_5$ system. The conductivity changes derived from a substitution of metal in octahedron unit MO$_6$ have also been reported on some mixed oxide or nitride systems.[34,35] The mobility of electron−hole pairs affects the photocatalysis because it affects the probability of electrons and holes reaching the reaction sites on the surface of the photocatalyst. Consequently, materials with a network of

2226 *J. Phys. Chem. B, Vol. 110, No. 5, 2006*

Abe et al.

corner-shared octahedral units of metal cations (TaO_6, NbO_6, or TiO_6) exhibit high photocatalytic activity, while materials without such a network show low activity. This hypothesis is supported by comparisons between (a) pyrochlore La_3TaO_7 and weberite La_3TaO_7 and (b) pyrochlore Gd_3TaO_7 and pyrochlore $Gd_2Ti_2O_7$. In the former case, in which both materials have the composition La_3TaO_7, weberite La_3TaO_7 with the zigzag chains formed by corner-shared TaO_6 octahedrons showed photocatalytic activity for overall water splitting, while pyrochlore La_3-TaO_7, with its mixed chain of TaO_6 and LaO_6, was inactive for the reaction. In the later case, in which both materials have the same pyrochlore crystal structure, $Gd_2Ti_2O_7$, with its network formed by corner-shared TiO_6 octahedrons, showed photocatalytic activity for overall water splitting, while the pyrochlore Gd_3TaO_7, with a mixed chain of TaO_6 and GdO_6, was inactive for the reaction. The presence of the network of corner-shared octahedrons is certainly one of the important factors governing the photocatalytic activity of the materials, while other factors, such as an appropriate band structure or a low efficiency of charge recombination, are undoubtedly required for the design of high active photocatalyst materials. Actually, most of the highly active photocatalysts such as $NaTaO_3$ possess the network of corner-shared octahedrons.

4. Conclusion

We prepared a series of R_3MO_7 and $R_2Ti_2O_7$ (R = Y, Gd, La; M = Nb, Ta) by the polymerized complex (PC) method and investigated their photocatalytic activity for splitting of pure water into H_2 and O_2. The crystal structures of R_3MO_7 changed with increasing ionic radius of the R^{3+} ion from cubic fluorite to cubic pyrochlore and, finally, to orthorhombic weberite. In the cases of La_3TaO_7 and La_3NbO_7, the phase transition from cubic pyrochlore to orthorhombic weberite was observed at around 1050 and 1000 °C, respectively. On the other hand, the crystal structures of $R_2Ti_2O_7$ changed from cubic pyrochlore to monoclinic perovskite with increasing ionic radius of R^{3+}. The photocatalytic overall water splitting into H_2 and O_2 proceeded over La_3TaO_7 and La_3NbO_7 (orthorhombic weberite structure), $Y_2Ti_2O_7$ and $Gd_2Ti_2O_7$ (cubic pyrochlore structure), and La_2-Ti_2O_7 (monoclinic perovskite structure). All of these photocatalysts possess a network of corner-shared octahedral units of metal cations (TaO_6, NbO_6, or TiO_6). All materials without such a network, namely Y_3TaO_7 and Y_3NbO_7 (fluorite-cubic structure), Gd_3TaO_7 and Gd_3NbO_7 (cubic pyrochlore structure), and La_3TaO_7 and La_3NbO_7 (cubic pyrochlore structure), were inactive for the photocatalytic water-splitting reaction. These results indicate the significant influence of crystal structure, in particular, the network of octahedral units of metal cations, on the photocatalytic activity of oxide semiconductor materials.

References and Notes

(1) Sato, S.; White, J. M. *Chem. Phys. Lett.* **1980**, *72*, 83−86.
(2) Domen, K.; Naito, S.; Soma, M.; Ohnishi, T.; Tamaru, K. *J. Chem. Soc., Chem. Commun.* **1980**, 543−544.
(3) Lehn, J.-M.; Sauvage, J.-P.; Ziessel, R. *Nouv. J. Chim.* **1980**, *4*, 623−627.
(4) Kudo, A.; Sayama, K.; Tanaka, A.; Asakura, K.; Domen, K.; Muruya, K.; Onishi, T. *J. Catal.* **1989**, *120*, 337−352.
(5) Inoue, Y.; Ogura, S.; Kohno, M.; Sato, K. *Appl. Surf. Sci.* **1997**, *121/122*, 521−524.
(6) Inoue, Y.; Kohno, M.; Kaneko, T.; Ogura, S.; Sato, K. *J. Chem. Soc., Faraday Trans.* **1998**, *94*, 89−94.
(7) Takata, T.; Shinohara, K.; Tanaka, A.; Hara, M.; Kondo, J. N.; Domen, K. *J. Photochem. Photobiol., A* **1997**, *106*, 45−49.
(8) Kim, H. G.; Hwang, D. W.; Kim, J.; Kim, Y. G.; Lee, J. S. *Chem. Commun.* **1999**, 1077−1078.
(9) Ishihara, T.; Nishiguchi, H.; Fukamachi, K.; Takita, Y. *J. Phys. Chem. B* **1999**, *103*, 1.
(10) Machida, M.; Yabunaka, J.; Kijima, T. *Chem. Mater.* **2000**, *12*, 812−817.
(11) Kudo, A.; Kato, H.; Nakagawa, S. *J. Phys. Chem. B* **2000**, *104*, 571−575.
(12) Abe, R.; Sayama, K.; Domen, K.; Arakawa, H. *Chem. Phys. Lett.* **2001**, *344*, 341−344.
(13) Kato, H.; Asakura, K.; Kudo, A. *J. Am. Chem. Soc.* **2003**, *125*, 3082−3089.
(14) Hwang, D. W.; Lee, J. S.; Li, W.; Oh, S. H. *J. Phys. Chem. B* **2003**, *107*, 4963.
(15) Abe, R.; Higashi, M.; Zou, Z.; Sayama, K.; Abe, Y.; Arakawa, H. *J. Phys. Chem. B* **2004**, *108*, 811−814.
(16) Abe, R.; Higashi, M.; Zou, Z.; Sayama, K.; Abe, Y. *Chem. Lett.* **2004**, *33*, 954−955.
(17) Maeda, K.; Takata, T.; Hara, M.; Saito, N.; Inoue, Y.; Kobayashi, H.; Domen, K. *J. Am. Chem. Soc.* **2005**, *127*, 8286−8287.
(18) Abe, R.; Sayama, K.; Sugihara, H. *J. Phys. Chem. B* **2005**, *109*, 16052−16061.
(19) Abe, R.; Takata, T.; Sugihara, H.; Domen, K. *Chem. Commun.* **2005**, 3829−3831.
(20) Yokogawa, Y.; Yoshimura, M.; Somiya, S. *Mater. Res. Bull.* **1987**, *22*, 1449.
(21) Yokogawa, Y.; Yoshimura, M.; Somiya, S. *Solid State Ionics* **1988**, *28*, 1250.
(22) Knop, O.; Brisse, F.; Castelliz, L. *Can. J. Chem.* **1996**, *47*, 971.
(23) Milanova, M. M.; Kakihana, M.; Arima, M.; Yashima, M.; Yoshimura, M. *J. Alloys Compd.* **1996**, *242*, 6.
(24) Kakihana, M.; Milanova, M. M.; Arima, M.; Okubo, T.; Yashima, M.; Yoshimura, M. *J. Am. Ceram. Soc.* **1996**, *79*, 1673.
(25) Okubo, T.; Kakihana, M. *J. Alloys Compd.* **1997**, *256*, 151.
(26) Higashi, M.; Abe, R.; Sayama, K.; Sugihara, H.; Abe, Y. *Chem. Lett.* **2005**, *34*, 1122.
(27) Domen, K.; Kudo, A.; Ohnishi, T. *J. Catal.* **1986**, *102*, 92.
(28) Harari, A. K.; Mazerolles, L.; Michel, D.; Robert, F. *J. Solid State Chem.* **1995**, *116*, 103.
(29) Ault, D.; Welch, J. E. *Acta Crystallogr.* **1966**, *20*, 410.
(30) Jehng, J.-M.; Wachs, I. E. *Chem. Mater.* **1991**, *3*, 100.
(31) Vendenboree, M. T.; Husson, E.; Chatry, J. P.; Michel, D. *J. Raman Spectrosc.* **1983**, *14*, 63.
(32) Scaife, D. E. *Sol. Energy* **1980**, *25*, 41.
(33) Zheng, C.; West, A. R. *J. Mater. Chem.* **1991**, *1*, 163.
(34) Bansal, C.; Kawanaka, H.; Takahashi, R.; Nishihara, Y. *J. Alloys Compd.* **2003**, *360*, 47.
(35) Ren, C.; Chan, D. S. H.; Wang, X. P.; Faizhal, B. B.; Li, M.-F.; Yeo, Y.-C.; Trigg, A. D.; Agarwal, A.; Balasubramanian, N.; Pan, J. S.; Lim, P. C.; Huan, A. C. H.; Kwong, D.-L. *Appl. Phys. Lett.* **2005**, *87*, 073506.